Crustal structure of the southernmost Ryukyu subduction zone: OBS, MCS and gravity modelling

Tan K. Wang,[1] Shen-Feng Lin,[1] Char-Shine Liu[2] and Cheng-Sung Wang[1,3]

[1]*Institute of Applied Geophysics, National Taiwan Ocean University, Keeling* 20224, *Taiwan. E-mail: tkwang@mail.ntou.edu.tw*
[2]*Institute of Oceanography, National Taiwan University, Taipei, Taiwan*
[3]*Now at: Division of General Education, Chin Min College, Toufin, Miaoli County, Taiwan*

SUMMARY

In 1995, a combined ocean-bottom-seismometric (OBS) and multichannel seismic (MCS) survey with strong air-gun shots was carried out in the southernmost Ryukyu subduction zone. A crustal velocity structure constructed from the layer-stripping Monte Carlo inversion of three OBS/MCS profiles and the associated density models inverted from gravity data in the SW end of the Ryukyu arc-trench system are presented. Parallel to the arc in the southernmost Ryukyu subduction system, the OBS/MCS profiles show sedimentary layers of the Hoping, Nanao and East-Nanao forearc basins from west to east, warping of the arc basement and buckling of the subducted slab beneath the Hoping basement rise. The arc-parallel variation of the crustal structure may result from increasing lateral compression westward due to oblique subduction of the Philippine Sea plate and collision with the Luzon arc near the northwestern edge of the forearc region. Northward subduction and arc-parallel compression of the slab also have generated thrust faulting along the subduction interface and strike-slip faulting within the subducted slab, respectively. On 2002 March 31, an earthquake with a moment magnitude of 6.84 was induced by buckling of the subducted slab and strongly affected cities within an epicentral distance of 100 km. The velocity-interface models, the density models and the focal mechanisms presented in this paper therefore suggest that earthquakes induced by slab buckling or arc-parallel compression have been stronger but less frequent than those generated by northward subduction in the Ryukyu seismogenic zone off Taiwan.

Key words: forearc system, Monte Carlo inversion, seismicity, subduction, travel-time inversion.

INTRODUCTION

Investigation of crustal structure in subduction zones is important to understand the correlation between seismogenic structure and seismicity and to evaluate the earthquake hazard for nearby areas. For example, the tsunamigenic potential is high in a subduction zone with a small accretionary prism and thin layers of subducted sediment (Polet & Kanamori 2000), while the activity of shallow earthquakes in a subduction zone depends on the thickness of the overriding plate, the subduction angle and the temperature at the forearc. Hyndman *et al.* (1997) proposed the up-dip and down-dip limits of seismogenic structures to be, respectively, the thrust contact with the overriding crust at 100–150°C and that with the forearc Moho at 350°C isotherms along the subduction interface. In general, the area shallower than the up-dip limit is the stable sliding friction regime of unconsolidated sediments, while a zone beyond the down-dip limit may consist of compacted and dehydrated sediments (Polet & Kanamori 2000). Through investigation of the seismicity and crustal structures in subduction zones, the up-dip limit of a seismogenic zone has been correlated with the deepest base of the accretionary prism (Kodaira *et al.* 2000; Tsuru *et al.* 2000).

Although the hypocentre distribution, focal mechanisms and seismic tomography have been widely used to delineate seismogenic structures, their resolution, accuracy and structural constraints are limited. These limitations are more serious for imaging crustal structures offshore, where seismic stations are sparse. On the other hand, with precise station relocation, an ocean bottom seismometric (OBS) can be deployed almost everywhere in an ocean and can receive both earthquake and control-sourced signals. Many OBS surveys have been conducted for imaging subduction systems in the circum-Pacific belt since the seismicity in this region represents more than 68 per cent of that in the global subduction zones according to the Council of the National Seismic System (CNSS).

In this paper, we first introduce the tectonic setting and seismicity in the Ryukyu subduction zone (Fig. 1), then analyze velocity models imaged by OBS surveys in the southernmost Ryukyu arc (the inset in Fig. 1), and finally present OBS velocity models and their correlation with the seismicity in the southernmost Ryukyu subduction zone. OBS imaging of the overlying and subducted plates, the subduction boundary, the subduction angle and the arc-parallel variation of the crustal structure presented in this paper enable us to determine both the dip limit and the lateral extent of the southernmost
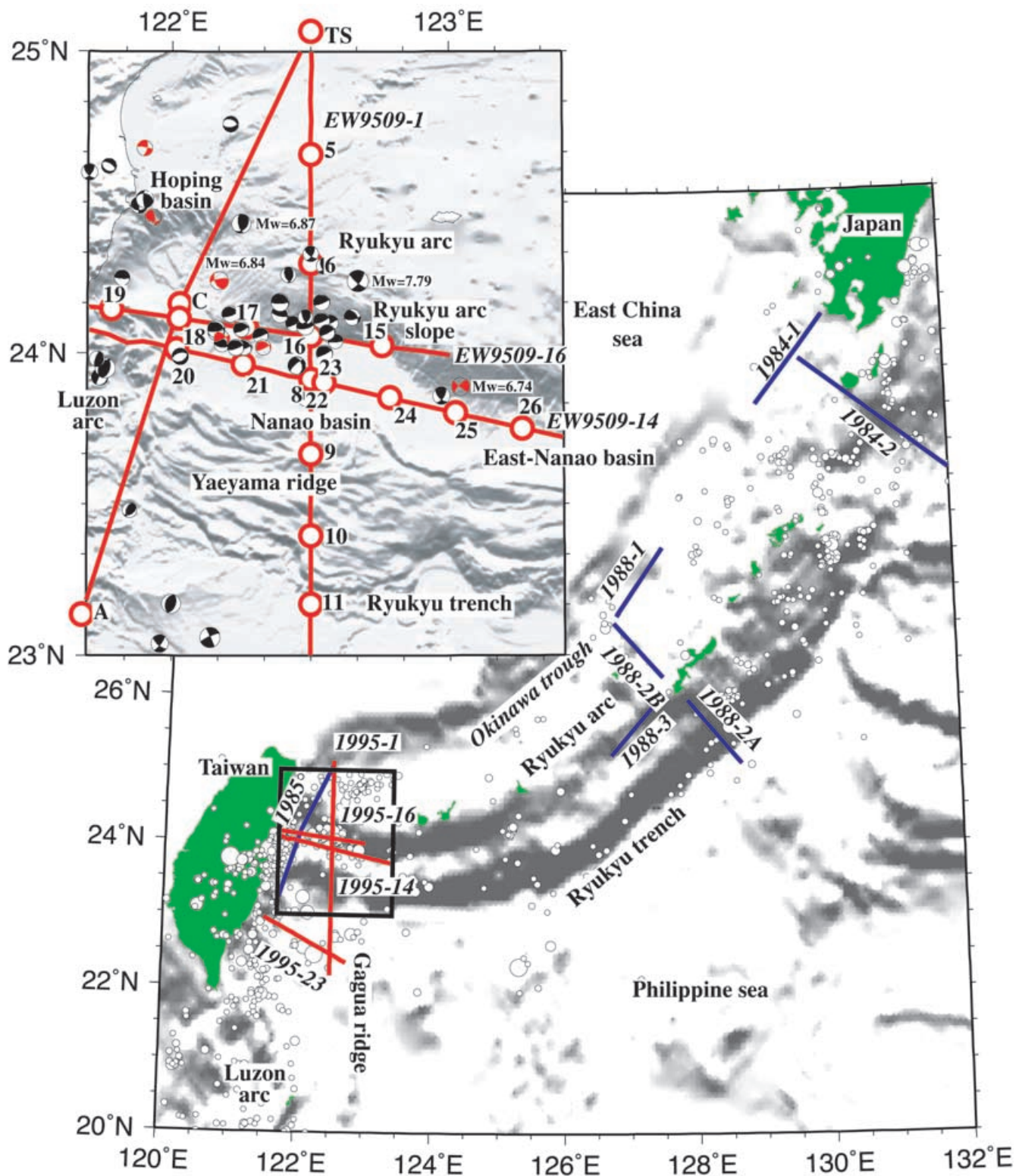
Figure 1. Bathymetry (shaded relief), epicentres (open circles) and ocean-bottom-seismometric (OBS) lines (thick solid lines) in the Ryukyu subduction zone. The bathymetry is plotted based on a 5-minute digital elevation model (DEM) of the NGDC (National Geophysical Data Center) TerrainBase. The epicentres are derived from the CNSS (Council of the National Seismic System) catalogue from 1963 onwards for magnitudes greater than 6 and depths less than 40 km. Two OBS experiments in the southernmost Ryukyu subduction zone (inside the black frame and enlarged in the upper left corner) were conducted in 1985 (Hagen *et al.* 1988) and 1995 (Liu *et al.* 1997). Other OBS surveys in the middle (Kodaira *et al.* 1996) and northernmost (Iwasaki *et al.* 1990) Ryukyu subduction zones are denoted by the years 1988 and 1984, respectively, when they were conducted. In the inset, the bathymetry is plotted from a DEM (Liu *et al.* 1998), while the darkened quadrants of the focal mechanisms (Kao *et al.* 1998 and Broadband Array in Taiwan for Seismology) show the first motion of the compressional wave. Four strong earthquakes are labelled with their moment magnitudes. Three OBS lines (EW9509-1, EW9509-14 and EW9509-16) connected by OBS stations (open circles) are investigated in this study.

Ryukyu seismogenic zone. Furthermore, by incorporating 3-D crustal interfaces from OBS profiles and earthquake focal mechanisms, we evaluate earthquake hazards due to subduction and collision in the southernmost Ryukyu arc.

TECTONIC SETTING, SEISMICITY AND OBS IMAGING IN THE RYUKYU SUBDUCTION ZONE

The Ryukyu subduction system consists of an arc, forearc and trench extending from Japan to Taiwan (Fig. 1). Northwestward subduction of the Philippine Sea plate (PSP) beneath the Eurasian plate in the NW portion of the circum-Pacific belt is the main tectonic motion generating high seismicity in the Ryukyu seismogenic zone. However, the tectonic and seismic characteristics vary from the northernmost Ryukyu subduction system to the southernmost Ryukyu subduction system. In the northernmost Ryukyu subduction system near the Japan island arc, the dip angle of the Wadati-Benioff zone is about 70 degrees with earthquake mechanisms indicating down-dip extension to depths of 80–120 km (Kao & Chen 1991). On the basis of OBS imaging conducted in 1984, the subduction angle in the crust varied from about 5 degrees to 10 degrees below the southeastern part of the sedimentary wedge (Iwasaki *et al.* 1990). In the middle Ryukyu subduction system, the dip angle of the Wadati-Benioff zone is 40–50 degrees, and OBS imaging conducted in 1988 showed a uniform angle of subduction of about 5 degrees (Kodaira *et al.* 1996). Although the dip angle of the Wadati-Benioff zone in the southernmost Ryukyu is similar to that in the middle Ryukyu, down-dip extension and the frequent shallow earthquakes in the southernmost Ryukyu are the same as those found in the northernmost Ryukyu. Through analysis of the earthquake mechanisms, the seismogenic interface in the southernmost Ryukyu has been determined to extend from 10 to 35 km in depth, while those in the middle and northernmost Ryukyu were found to be 30–50 km in depth (Kao *et al.* 1998). Furthermore, three forearc basins (the inset of Fig. 1) were imaged in the southernmost Ryukyu arc (Font *et al.* 2001), but they have not been reported for the middle and northernmost Ryukyu arc. The differences in the northernmost, middle and southernmost Ryukyu subduction systems result from the distinct regional tectonics. For example, compression along the subduction direction but extension along the trench occurs in most of the subduction zones (Jarrard 1986), but arc-parallel compression due to on-going collision or the westward component of oblique subduction due to termination of subduction was found in the SW end of the Ryukyu (Lallemand *et al.* 1999).

The earliest OBS survey in the southernmost Ryukyu was conducted near the coast of Taiwan in 1985 (ACTS OBS profile shown in the inset of Fig. 1). Due to the lack of a strong air gun, the result only showed northward thickening of the upper crust in the forearc region (Hagen *et al.* 1988). In 1995, a combined OBS and multichannel seismic (MCS) survey using strong air-gun shots (8640 in^3 from R/V Maurice Ewing) was conducted off Taiwan (Liu *et al.* 1997). Travel-time inversion of the velocity-interface structure parallel to the subduction direction (EW9509-1) showed a thick accretionary prism beneath the Yaeyama ridge and a slab kink due to subduction below the Nanao basin (Wang *et al.* 2001). Furthermore, the westward extension of the Ryukyu arc basement beneath the Hoping basin and intra-crustal interfaces dipping westward below the Hoping basin were imaged from the EW9509-14 profile (McIntosh & Nakamura 1998) and the EW9509-16 profile (Wang & Chiang 1998), respectively. The four OBS profiles in the SW end of the Ryukyu (the inset of Fig. 1) also revealed strong lateral variations

of the crustal interfaces west of the Nanao basin (Lin 2000). In this paper, the sedimentary and crustal structures along these OBS/MCS profiles are further investigated by means of Monte Carlo inversion of the model uncertainty as well as the gravity modelling. Structural interfaces in 3-D are also established by incorporating these profiles and for investigating the lateral variation of the subduction structures.

TRAVEL-TIME AND GRAVITY MODELLING

Travel-time modelling of the velocity-interface structures along three OBS/MCS profiles in the southernmost Ryukyu subduction system consists of three major steps. Based on MCS and OBS arrivals, three sedimentary layers and three crustal layers of the velocity-interface models are first constructed layer by layer (Zelt & Smith 1992). An adapted Monte Carlo inversion using the ray-tracing scheme of Zelt & Smith (1992) is then applied to obtain the model velocity, the interface geometry and their uncertainties. Finally, the structural constraints and the model uniqueness are evaluated from the ray coverage and the minimum number of model parameters, respectively. Due to the limitation of ray coverage in the model boundary, a gravity inversion (Webring 1985), with the initial density models converted from the velocity models, is employed to constrain the lower crust and the upper mantle.

Layer-stripping inversion

Travel times of MCS data are used for layer-stripping inversion of sedimentary structures in the southernmost Ryukyu subduction zone. For example, the stacked MCS section of profile EW9509-14 shown in Fig. 2(a) (Font *et al.* 2001) shows clear sedimentary strata in the Hoping, Nanao and East-Nanao forearc basins from west to east. By considering the reflected and refracted arrivals in the MCS and OBS data, the velocities (the contours in Fig. 2c) and the interfaces (the thick lines in Fig. 2c) of the forearc basins are well constrained with a rms travel-time error of less than 0.1 s. Fig. 2(b) demonstrates that the calculated arrivals of the zero-offset reflections are consistent with the stacked MCS section. In particular, the minimum number of velocity grids (the small solid circles in Fig. 2c) is achieved to accommodate refracted rays from the sparse OBS stations since the model velocity cannot be fully constrained by the travel times of the stacked MCS section. The sedimentary velocities of about 1.7–2 km s^{-1} (Quaternary to Pliocene), 2.3–3 km s^{-1} and 3–4.5 km s^{-1} obtained in this study are similar to those about 200 km east of the study area in the SW Ryukyu arc (Park *et al.* 1998).

Due to the low signal-to-noise ratio in the deep section of the MCS data, we use only OBS arrivals to invert the arc basement and the subducted slab layer by layer. In the following, we demonstrate how the OBS arrivals constrain the structures of the Ryukyu arc and the PSP along profiles EW9509-14 and EW9509-16. Examples of travel-time modelling along profile EW9509-1 have been given in detail by Wang *et al.* (2001).

Ryukyu arc

The upper velocities of the arc basement, covered by the refracted rays (the solid lines in Figs 3a–5a), are well constrained by the first arrivals of Pg2 in the OBS data (Figs 3b–5b). We also find that an intra-crustal interface between the arc basement and the PSP dips eastward (15–20 degrees) below the western portion of the Nanao basin (Figs 3a and 4a). The portion of this dipping interface is imaged by reflected arrivals (*Pc2P*) at the western offset of station 22 along
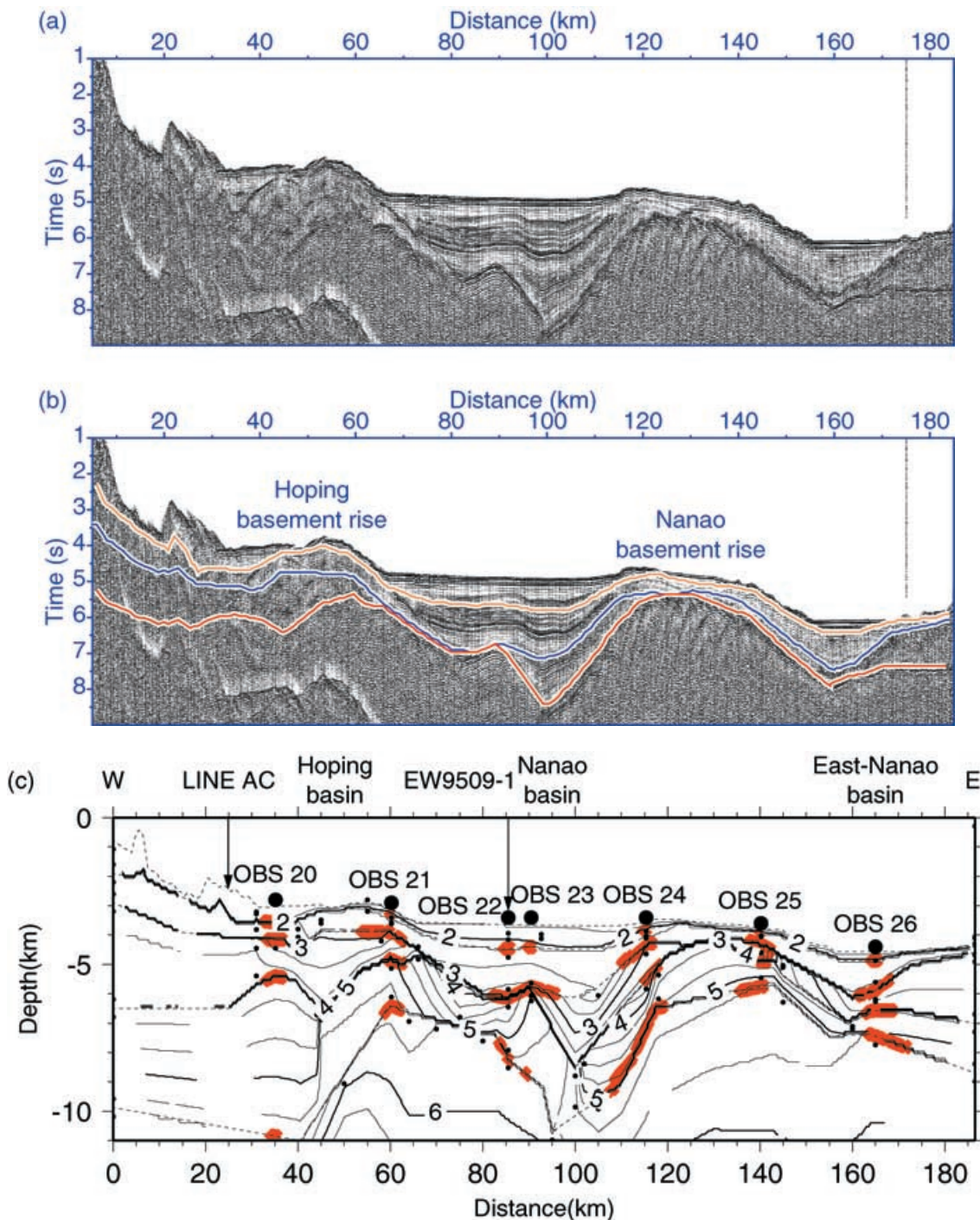
Figure 2. (a) Stacked MCS data along the EW9509-14 profile in the southernmost Ryukyu forearc basins, (b) the calculated travel times (solid lines) superimposed on the stacked section and (c) the associated velocity-interface model developed in this study. The thick lines and the small solid circles in (c) are reflection points and velocity grids in the OBS data modelling, respectively. The contour interval in (c) is 0.25 km s^{-1}. The velocity contours of 2.25, 3 and 4.5 km s^{-1} in (c), which correspond to three sedimentary layers in the forearc basins, clearly match the reflecting signals in (a) except beneath the Nanao basin and west of OBS station 20.

profile EW9509-14 (Fig. 3b) and at the eastern offset of station 17 along profile EW9509-16 (Fig. 4b).

Philippine Sea plate

The PSP is partially constrained by rays reflected from the Moho (the dashed lines through the PSP in Figs 3a–5a) and refracted through the oceanic crust (*Pg3*) and the upper mantle (*Pn*) as shown

in Fig. 5(a). Unfortunately, the depression of the PSP below the Nanao basin cannot be imaged by OBS arrivals from station 22 (Fig. 3). However, the velocity and interface constraints (Fig. 9a) and the intersection of the EW9509-1 profile (Fig. 7b) at station 22 still support the slab depression. On the other hand, the buckling of the slab beneath the Hoping basement rise (a basement high between the Hoping and Nanao basins) is identified by *PmP* arrivals at the
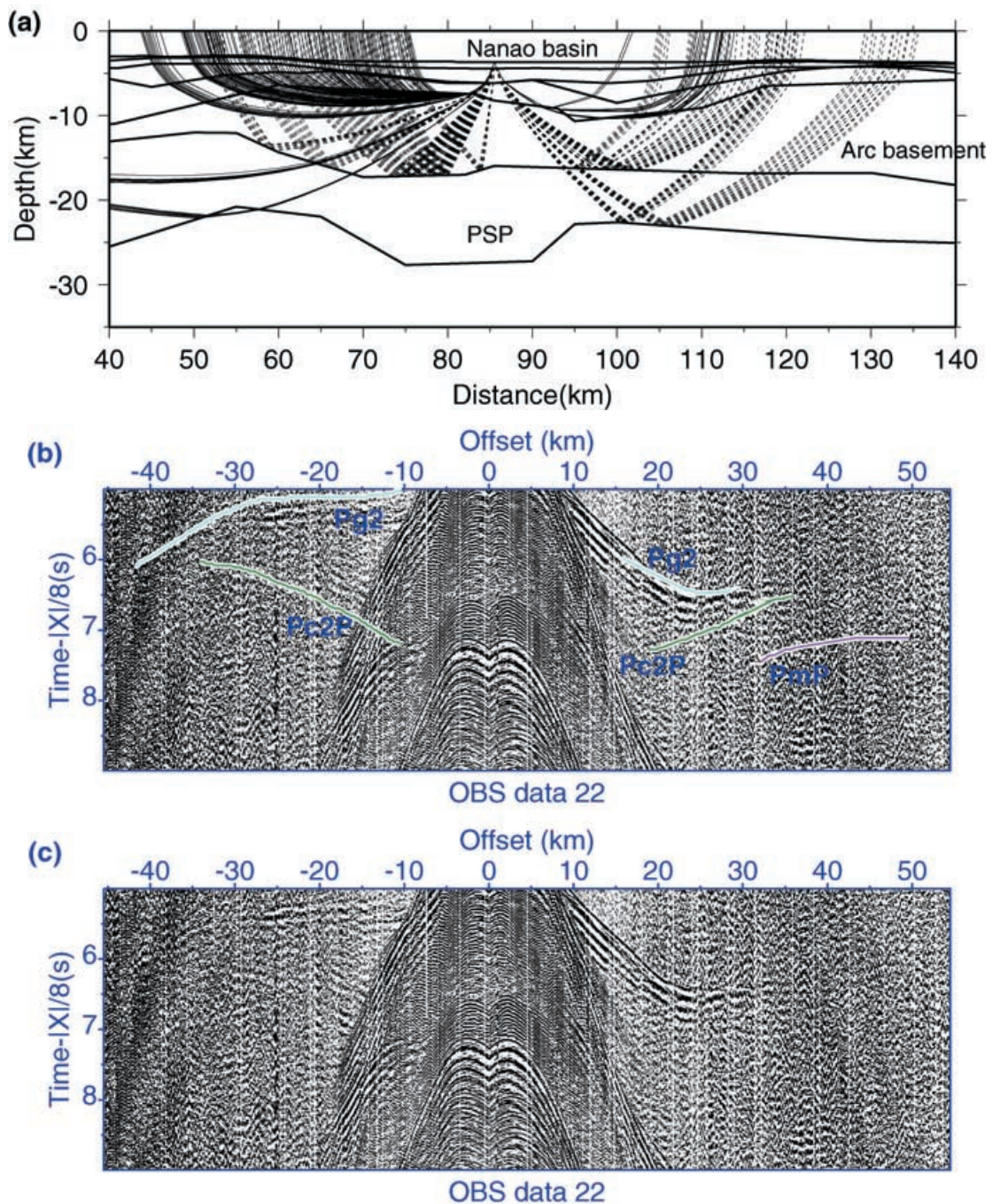
Figure 3. (a) Refracted (solid lines) and reflected (dashed lines) rays arriving at station 22 and travelling in the arc basement and the PSP along the EW9509-14 profile; (b) calculated arrivals (solid lines) superimposed on the OBS data; and (c) the vertical component of the OBS data from station 22. The phases of Pg2 and *Pc2P* in (b) indicate refractions through the arc basement and reflections from the top of the PSP, respectively. Reflections from the Moho (*PmP*) in (b) are considered to demonstrate the ray coverage in (a).

eastern offset of station 17 (Fig. 4b) and weak arrivals of *Pg3*, *Pn* and *PmP* at the western offset of station 15 (Fig. 5b) along profile EW9509-16.

The rms errors of refracted and reflected arrivals received from each station are generally less than 0.1 s for each layer along the OBS profiles.

Monte Carlo modelling

To determine the velocity and interface uncertainties of the model, a search of the best model parameters similar to the Monte Carlo in-

version is conducted. Monte Carlo modelling is applied in this study due to its capability to quantify model parameters involving random behavior (Zaidi 1999; Spada 2001). For simplicity, only one parameter, a velocity or an interface depth, is tested at one time within a geologically reasonable range to minimize the traveltime residuals and to maximize the ray coverage. In this study, the uncertainties of velocities and interfaces are evaluated when the rms traveltime error is about 20 ms, because a shift of 20 ms should be detected in the OBS data with good signal quality (Christeson *et al.* 1999). Furthermore, the increments of the velocity and the interface during Monte Carlo
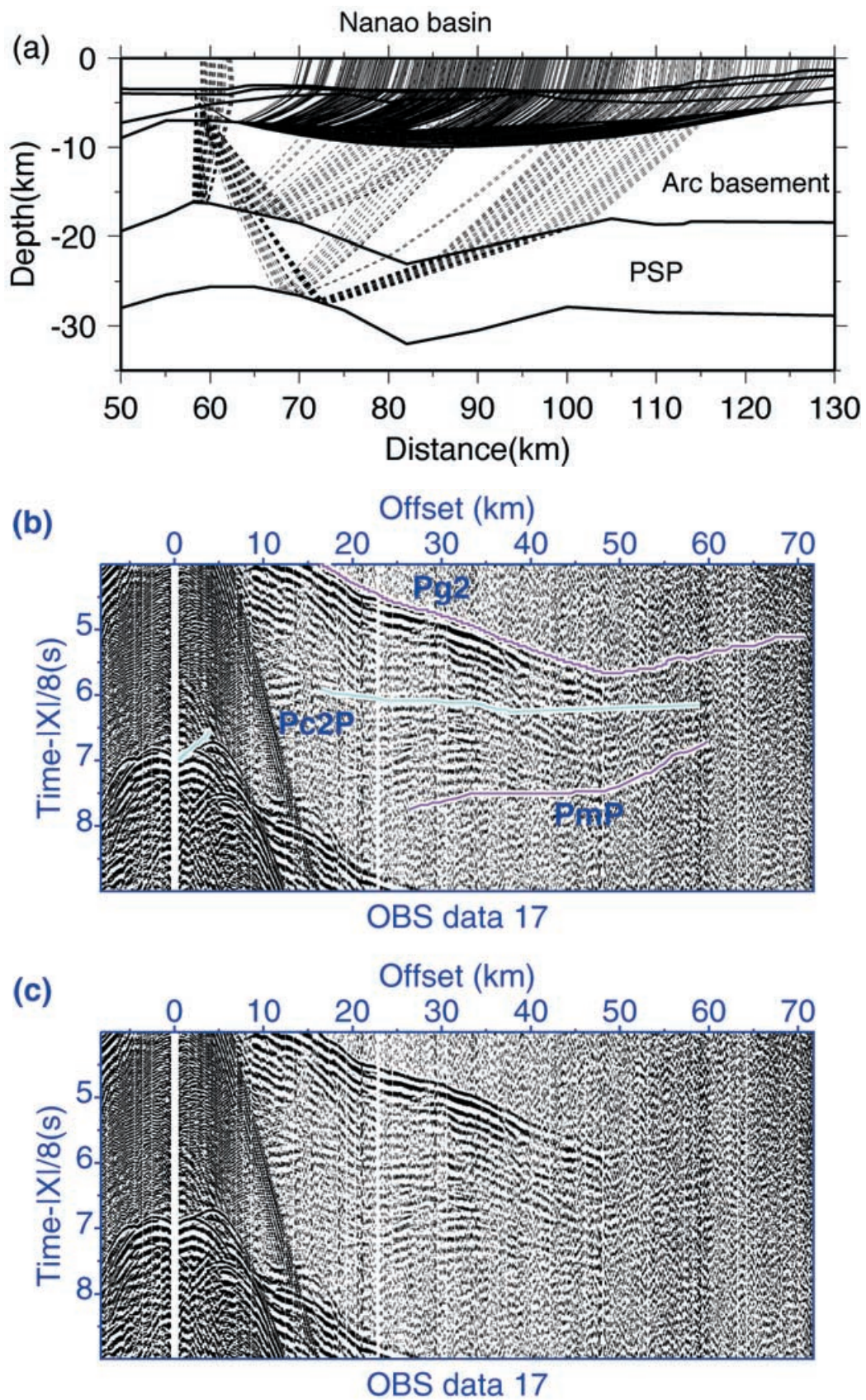
Figure 4. (a) Refracted (solid lines) and reflected (dashed lines) rays arriving at station 17 and travelling in the arc basement and the PSP along the EW9509-16 profile; (b) calculated arrivals (solid lines) superimposed on the OBS data; and (c) the vertical component of the OBS data from station 17. The nomenclature of the phases in (b) is the same as that in Fig. 3.
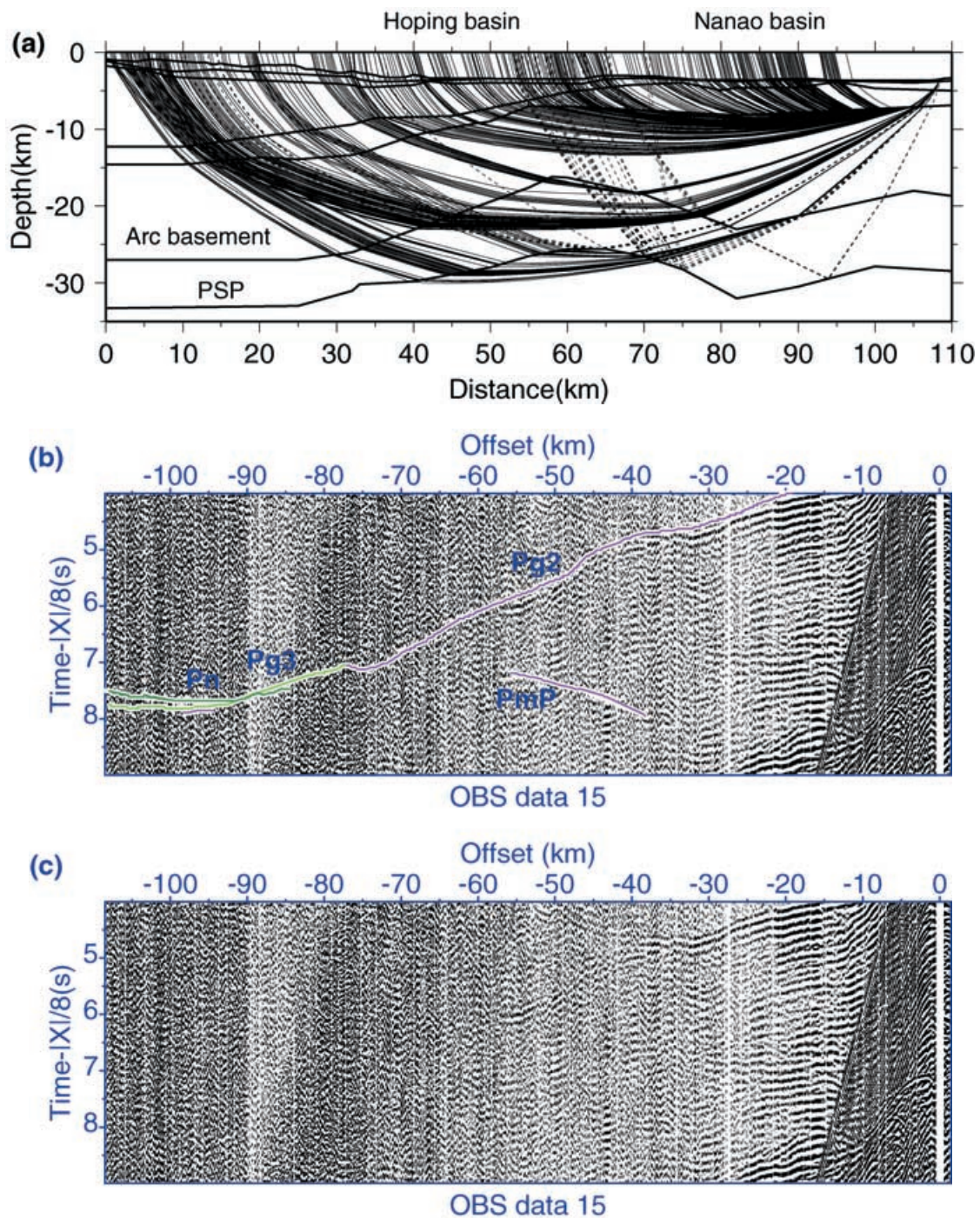
Figure 5. (a) Refracted (solid lines) and reflected (dashed lines) rays arriving at station 15 and travelling in the arc basement and the PSP along the EW9509-16 profile; (b) calculated arrivals (solid lines) superimposed on the OBS data; and (c) the vertical component of the OBS data from station 15. Refractions through the PSP (*Pg3*), refractions through the upper mantle (*Pn*), and reflections from the Moho (*PmP*) in (b) are not used in inversion but are considered to demonstrate the ray coverage in (a).

modelling are 0.01 km s^{-1} and 0.01 km, respectively. Velocity uncertainty along profile EW9509-14 (Fig. 6) is found to be generally less than 0.25 km s^{-1} except below the Nanao basin where it reaches 0.45 km s^{-1}. As for the interface uncertainty along profile EW9509-14, it is found to generally be less than 0.5 km except at the Moho below the western portion of the Nanao basin. The high uncertainty level of the model parameters may be due to the complex structures below the Nanao basin. The uncertainties of the velocity-interface

models along other OBS profiles are similar to those along profile EW9509-14.

Ray coverage and minimum number of model parameters

As shown in Figs 7(a), 8(a) and 9(a), the model constraints are demonstrated by the coverage of refracted rays (colour shaded) and reflection points (thick lines), while velocity grids (small circles)
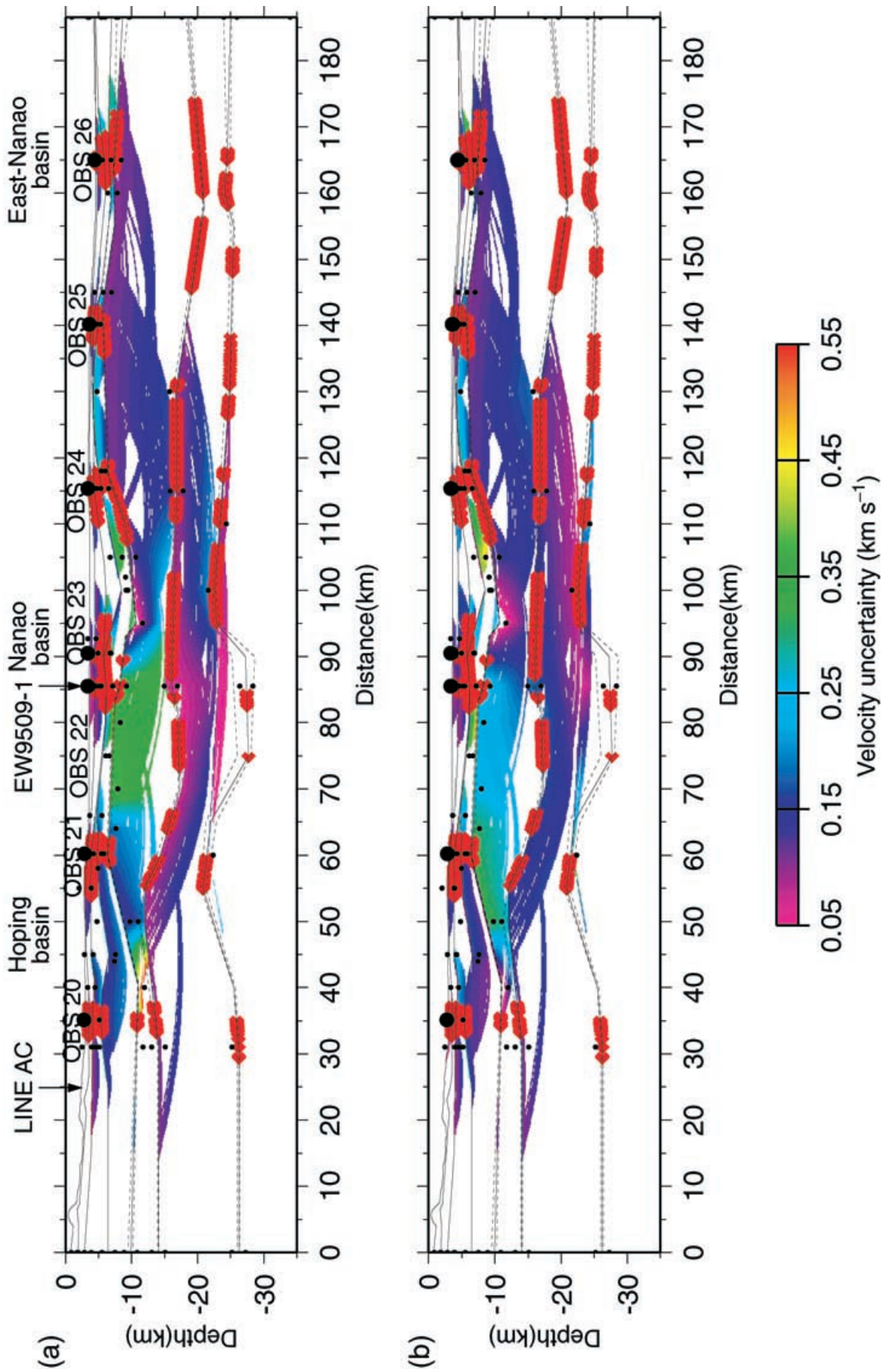
Figure 6. (a) The upper limit of the velocity uncertainty and (b) the lower limit of the velocity uncertainty along the EW9509-14 profile. The velocity uncertainty is constrained by refracted rays through their lowest layers. The solid lines and the dashed lines denote the interfaces of the model and the associated depth uncertainties, respectively. The thick lines and the small circles are reflection points of the selected arrivals and velocity grids, respectively.
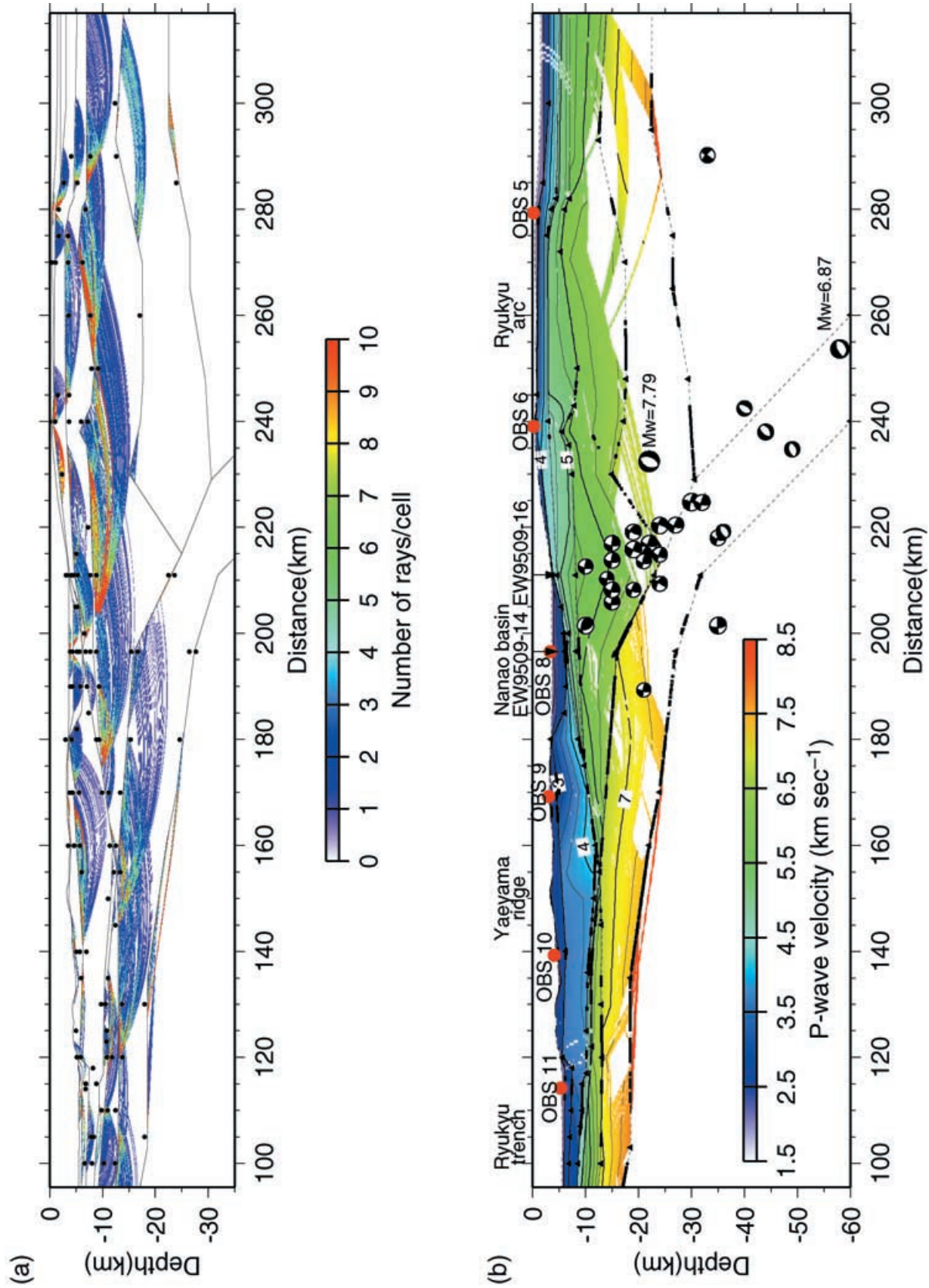
Figure 7. (a) The number of rays in each cell (colour shaded) refracted through their lowest layers along profile EW9509-1. The dimensions of the cell are 0.25 km and 0.05 km along the length and the depth of the model, respectively. Velocity grids are displayed as small solid circles. (b) A *P*-wave velocity-interface model along profile EW9509-1 in the southernmost Ryukyu subduction zone. The black triangles and the thick lines are interface grids and reflection points of the selected arrivals, respectively. Focal spheres (Kao *et al.* 1998) are projected onto the seismic profile, and their darkened quadrants show the first motion of the compressional wave.
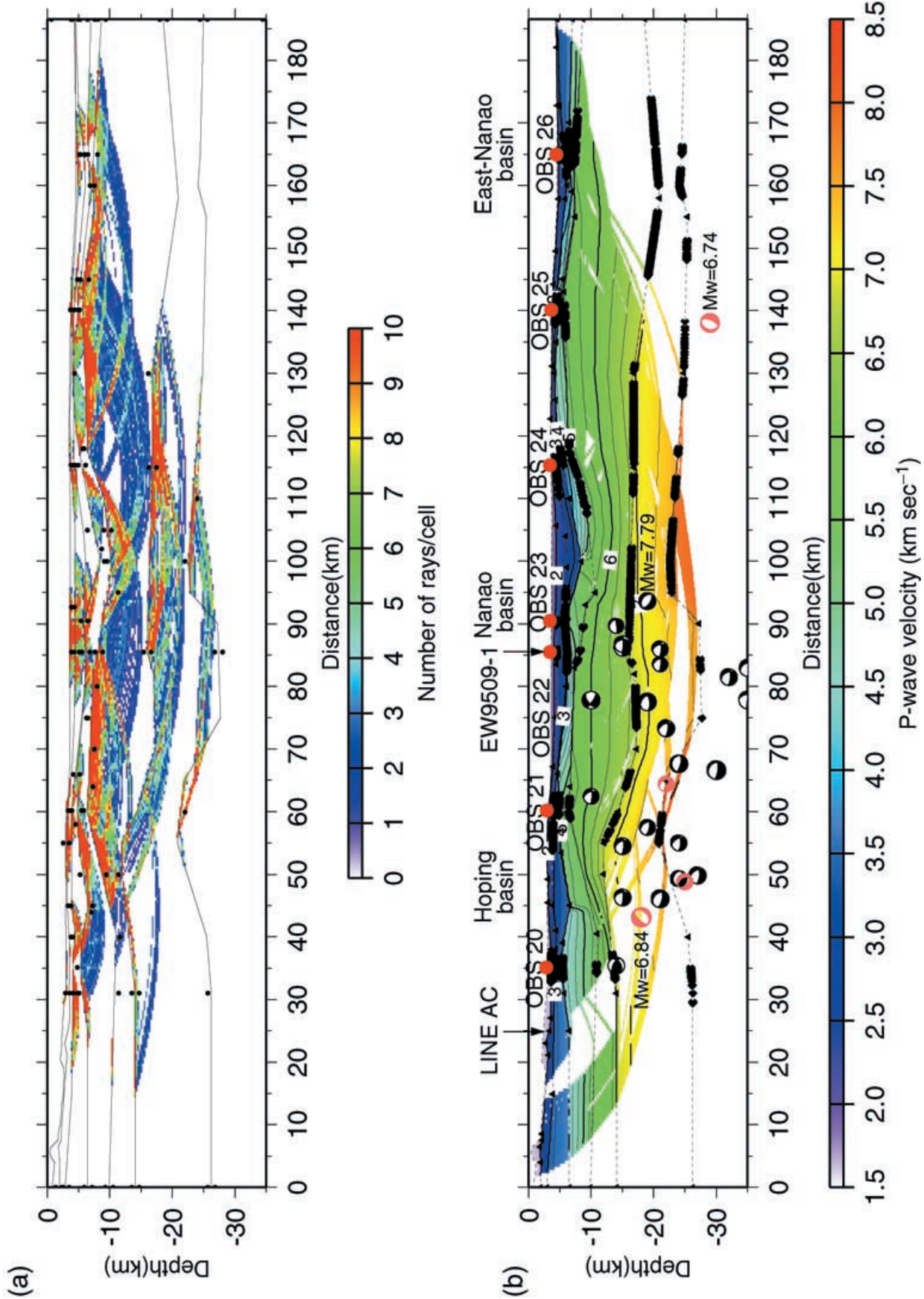
Figure 8. (a) The number of rays in each cell (colour shaded) refracted through their lowest layers along profile EW9509-14. (b) A *P*-wave velocity-interface model along profile EW9509-14 in the southernmost Ryukyu subduction zone. Symbols similar to those in Fig. 7 are used except that the focal mechanisms shown in red colour are obtained from Broadband Array in Taiwan for Seismology.
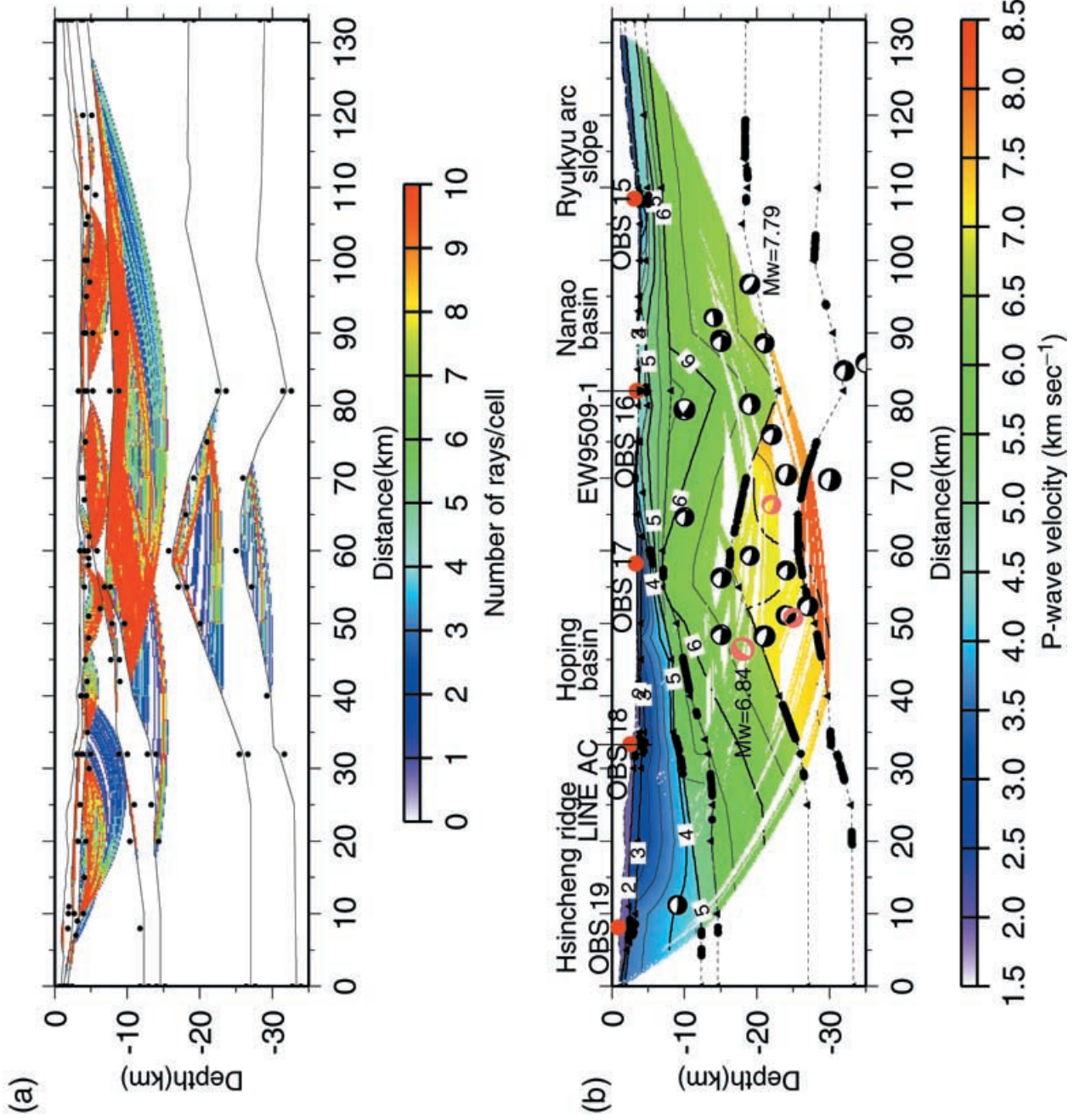
Figure 9. (a) The number of rays in each cell (colour shaded) refracted through their lowest layers along profile EW9509-16. (b) A *P*-wave velocity-interface model along profile EW9509-16 in the southernmost Ryukyu subduction zone. Symbols similar to those in Fig. 8 are used.

and interface grids (triangles) are used to evaluate the minimum number of model parameters. Rays refracted through their lowest layer are investigated because a layer-stripping inversion is applied to constrain the velocity of one layer at a time. Full coverage of the refracted rays in the sedimentary layers and the Ryukyu arc basement is obtained, while refracted rays which travel through the PSP occur only south of the Ryukyu arc (Fig. 7a) and below the Hoping basement rise (Figs 8a and 9a). On the other hand, most of the sedimentary interfaces are constrained by MCS/OBS reflected arrivals (Fig. 2), but the Moho and the bottom of the Ryukyu arc basement are mostly imaged by OBS reflected arrivals. Furthermore, there are at least two advantages of considering a minimum number of model parameters. The first advantage is to enhance the efficiency of layer-stripping inversion and Monte Carlo modelling although it is difficult to minimize the number of the model parameters before inversion. The second advantage of minimizing the number of grids is to avoid the model over-fitting and to reduce the model non-uniqueness. In this study, by comparing the coverage of rays and the reflection points with the distribution of the velocity and interface grids (Figs 7a, 8a and 9a), a minimum number of model parameters is achieved.

Gravity inversion

Since the subducted slab greater than 25 km depth or west of the Nanao basin is unconstrained in the velocity models of OBS/MCS profiles (Figs 7, 8 and 9), a gravity inversion is employed to better constrain the models. We first convert the velocity model to a density model by using the scheme provided by Zelt & Smith (1992). The unconstrained portions of the initial density model are then inverted by considering the gravity data collected along the same MCS/OBS profiles during 1995 Ewing cruise. After inversion, the rms errors of the gravity anomaly are generally less than 5 mGal along three profiles (Figs 10a, 11a and 12a). Furthermore, the densities at intersection of three profiles are consistent after gravity inversion.

RESULTS AND DISCUSSION

Velocity-interface structures and density models along the subduction direction, parallel to the arc, and their 3-D crustal interfaces in the southernmost Ryukyu seismogenic zone are presented in this section. Their tectonic implications and their application to earthquake hazards by considering the focal mechanisms are also described below.

Structure along the subduction direction

A *P*-wave velocity model along EW9509-1 (Fig. 7b) shows that thick sediment has accumulated with the maximum thickness of 4 km and 8 km in the Ryukyu trench (*P*-wave velocity = 1.6–4.5 km s^{-1}) and the Yaeyama accretionary prism (*P*-wave velocity = 1.8–4.5 km s^{-1}), respectively. The accumulation of these sedimentary layers can be attributed not only to the abundant supply of sediment from the Taiwan orogen, but also to off scarping and accretion from northward subduction of the PSP underneath the Ryukyu arc. However, due to the thick sediment and the large accretionary prism, earthquakes have rarely ruptured through to the sea floor and generated tsunamis (Polet & Kanamori 2000). The low tsunamigenic potential in the southernmost Ryukyu forearc region is further supported by the small number of earthquakes occurring near the trench (Fig. 1).

North of the prism, the Ryukyu arc forms the backstop of the accretionary wedge (Fig. 7b). The Ryukyu arc basement is 20–25 km thick with a velocity of 4.5–7.75 km s^{-1} north of the forearc basins and is 8–15 km thick with a velocity of 4.5–6.75 km s^{-1} beneath the forearc basins, and it extends southward, in a wedge-like shape, beneath the Yaeyama accretionary prism. The frontal wedges (the accretionary prism and the backstop) are thickened and shortened by thrust faulting near the plate interface.

As for the PSP model, the thickness of the subducted slab is 8-11 km, and the subduction angle increases northward from 5 degrees near the trench to 25 degrees underneath the overriding crust. Since the seismogenic zone extends from the deepest base of the accretionary prism to the Moho of the overriding crust along the subduction boundary (Hyndman *et al.* 1997; Kodaira *et al.* 2000; Tsuru *et al.* 2000), the width and the depth of the seismogenic zone along the subduction direction in the southernmost Ryukyu are about 75 km and 15–30 km, respectively. The abrupt down-dip increase of the subduction angle along EW9509-1 is similar to the subduction kink in the Cascadia off California, where post-subduction deformation and lower crustal shortening due to compression have occurred (Leitner *et al.* 1998). On the other hand, the density model just beneath the subduction kink along profile EW9509-1 (the shaded area in Fig. 10b) indicates a relatively low density of 2960 kg m^{-3} that cannot be well resolved by the velocity model (Fig. 7b). This low-density block may also imply the fracture due to the subduction kink of the PSP below the Nanao basin.

Structure parallel to the arc

The Hoping, Nanao and East-Nanao basins, with sediments (*P*-wave velocity = 1.6–3 km s^{-1}) up to 4 km thick (Fig. 2), are clearly imaged from west to east in the southernmost Ryukyu arc although the forearc basins are not common in other subduction systems (e.g. NE Ryukyu). Underneath these forearc basins, a layer with velocities of 3–4.5 km s^{-1} shows a gentle undulation beneath the eastern portion of the Nanao basin and the western portion of the East-Nanao basin (Fig. 2c). Between these basins, the Hoping and Nanao basement rises of the Ryukyu arc are imaged with *P*-wave velocities greater than 4.5 km s^{-1}. The velocity (3–4.5 km s^{-1}) undulation beneath the forearc basins can be attributed to subducted/underplated sediment (Wang & Pan 2001) that is dewatered and scraped off from the downgoing oceanic plate.

The reasons for the separation of the Hoping and Nanao basins or the formation of the Hoping basement rise are investigated based on the OBS velocity models along EW9509-14 and EW9509-16. Velocity (3–4.5 km s^{-1}) undulation beneath the western portion of the Nanao basin (Fig. 8b) may result from the interaction between the arc basement and the forearc basin. Beneath the Hoping basin and in the Hsincheng ridge, the compacted sediment and the upper crust (*P*-wave velocity = 3–5.5 km s^{-1}) are westward thickening (Figs 8b and 9b). From imaging of the arc basement and the PSP, an intracrustal interface (*P*-wave velocity = 6.75 km s^{-1}) dips eastward (15–20 degrees) below the western portion of the Nanao basin and dips westward (5–20 degrees) below the Hoping basin. Furthermore, the Moho of the PSP (*P*-wave velocity = 7.75 km s^{-1}) below the Hoping basement rise is shallower than that below the Hoping and Nanao basins. Therefore, we infer that, due to the westward component of the PSP subduction or arc-parallel compression within the subducted slab (Kao *et al.* 1998), slab buckling has generated the Hoping basement rise and has separated the Hoping and Nanao basin in the southernmost Ryukyu forearc region.
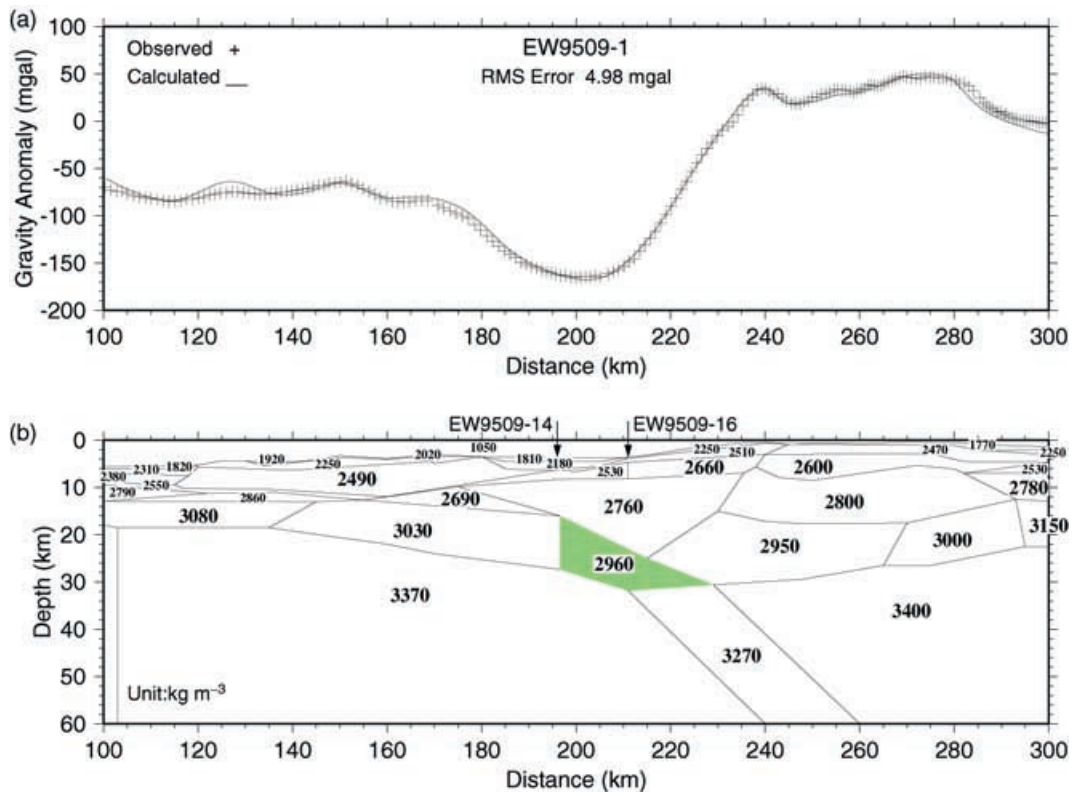
Figure 10. (a) Observed and calculated gravity anomalies, and (b) a density model along profile EW9509-1. The density model of (b) is constructed from the velocity model shown in Fig. 7(b).
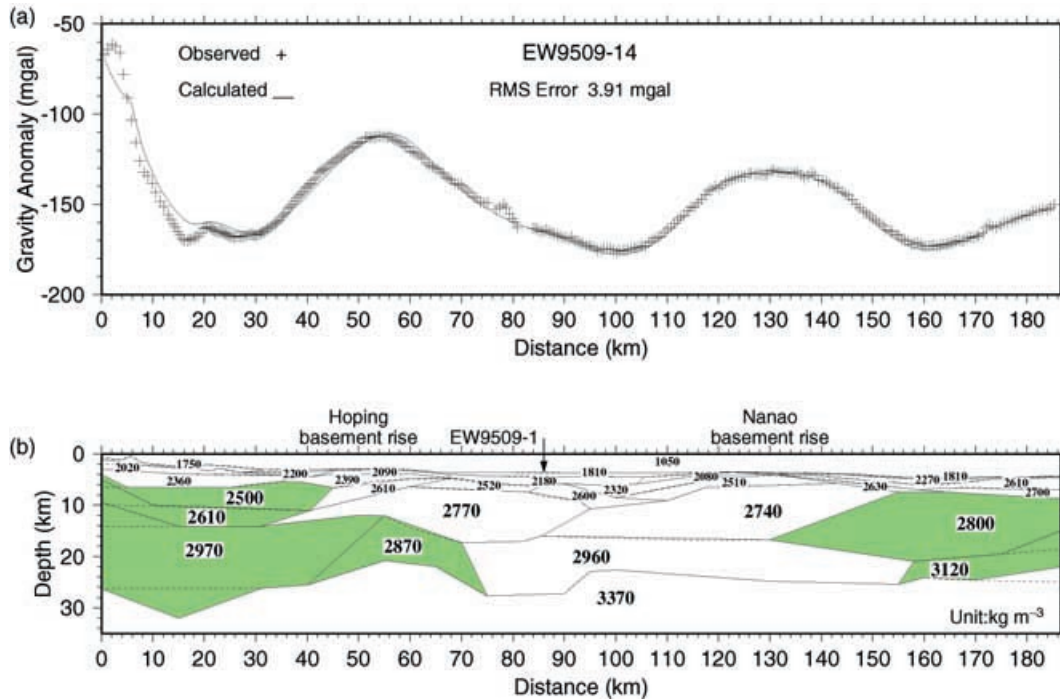

Figure 11. (a) Observed and calculated gravity anomalies, and (b) a density model along profile EW9509-14. The initial model of (b), the un-shaded region and the dashed lines, is constructed from the velocity model shown in Fig. 8(b).
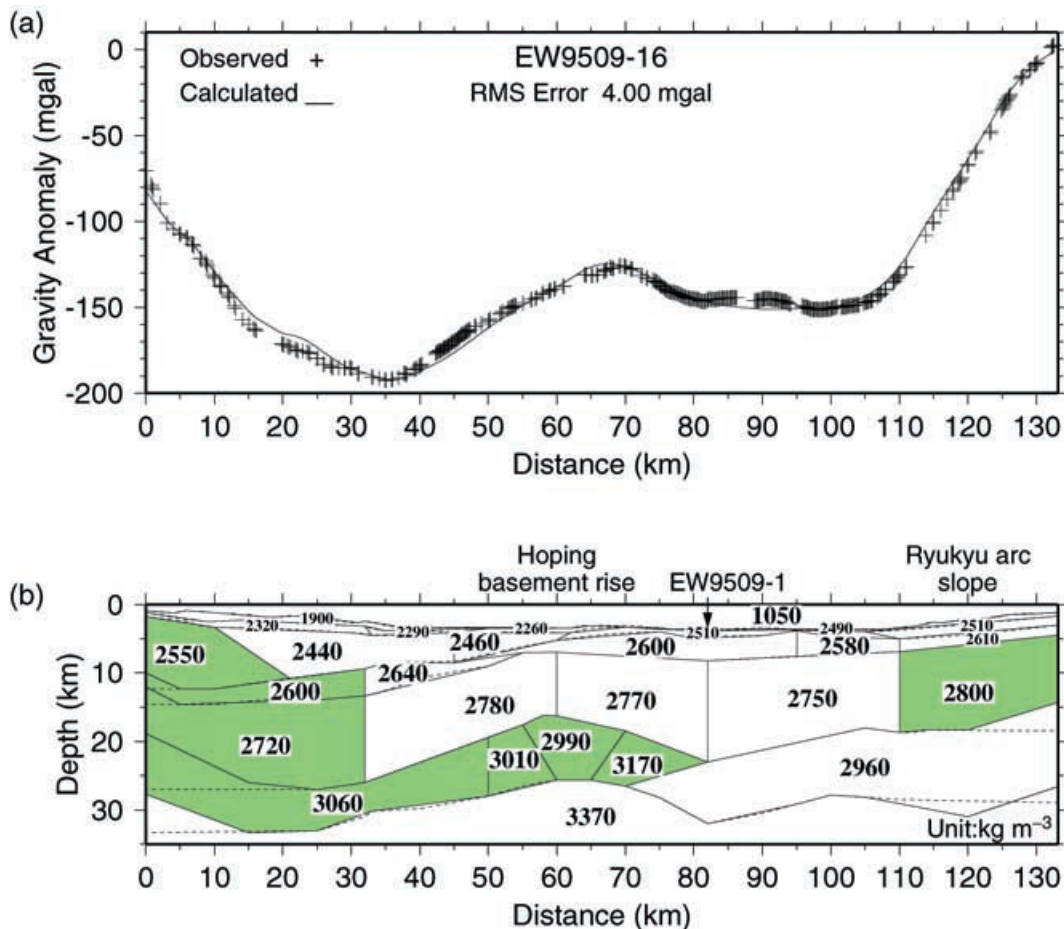
Figure 12. (a) Observed and calculated gravity anomalies, and (b) a density model along profile EW9509-16. The initial model of (b), the un-shaded region and the dashed lines, is constructed from the velocity model shown in Fig. 9(b).

The slab buckling is observed more evidently from the density models. Below the Hoping basement rise, the relatively low density of 2870 kg m^{-3} along profile EW9509-14 (the shaded area in Fig. 11b), the relatively low density of 2990–3010 kg m^{-3} and the relatively high density of 3170 kg m^{-3} along profile EW9509-16 (the shaded area in Fig. 12b) are converted from the velocity-interface models (Figs 8b and 9b). The low density of the subducted slab is attributed to the fracture upon the slab buckling whereas the high density of the slab may have resulted from the arc-parallel compression within the slab. Furthermore, west of the Hoping basement rise, the relatively low densities (2500 kg m^{-3} and 2610 kg m^{-3} along EW9509-14 and 2600 kg m^{-3} and 2720 kg m^{-3} along EW9509-16) of the upper crust but the relatively high densities (2970 kg m^{-3} along EW9509-14 and 3060 kg m^{-3} along EW9509-16) of the lower crust are inverted from the gravity anomaly. The low density of the upper crust may be associated with the down warping of the slab, and the high density of the lower crust is due to the arc-parallel compression. It also can be seen that, below the Hoping basement rise and near the coast, the densities along profile EW9509-16 are generally about 100 kg m^{-3} greater than those along profile EW9509-14. This density variation may imply more arc-parallel compression or stronger buckling of the slab, along profile EW9509-16, at the front of the northward subduction of the PSP.

Relatively high densities and dipping interfaces at the western and eastern ends of profiles EW9509-14 and EW9509-16 are also found. Near the coastal region, a relatively high density of

2550 kg m^{-3} along EW9509-16 (Fig. 12b) is converted from the velocity-interface model (Fig. 9b). Furthermore, eastward dipping interfaces of the density models (dashed lines in Figs 11b and 12b), which cannot be imaged through seismic data, are inverted from the gravity high near the coast. The high density and the eastward dipping interfaces may be attributed to the ongoing exhumation of the subducted continental crust near the coast (Lin *et al.* 1998). On the other hand, due to the gravity high at the eastern ends of the profiles, the relatively high densities (2800 kg m^{-3} and 3120 kg m^{-3}) and the westward dipping interfaces are obtained. The high density and dipping interfaces at the eastern ends of the profiles may have resulted from the subduction of the Gagua ridge (Schnürle *et al.* 1998) that could be responsible for the separation of the Nanao and East-Nanao basins.

3-D Crustal interfaces

Four OBS/density models along profiles EW9509-1, EW9509-14 and EW9509-16 and ACTS (Figs 1, 7, 8 and 9) are incorporated by tying together the velocity and the interface depth at their intersection. Triangulation of the structural grids along the four profiles enables us to construct a 3-D model and to display it in the format of the Virtual Reality Modelling Language (VRML) for 3-D visualization and network access. In this paper, we only present the top and bottom of the subducted slab (blue and yellow
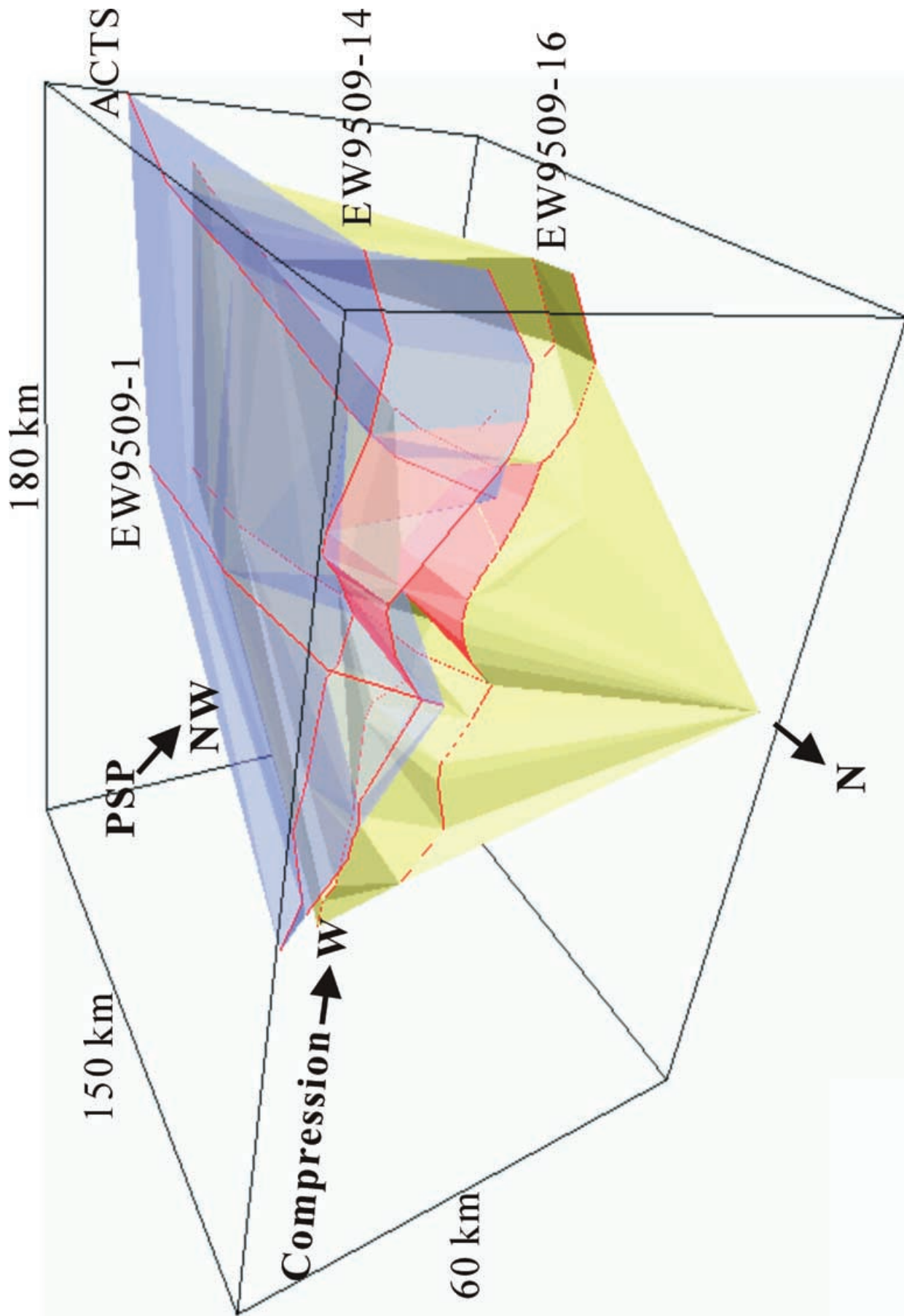
Figure 13. Top (blue) and bottom (yellow) of the subducted slab constructed from the velocity-interface models and the density models along profiles EW9509-1, EW9509-14, EW9509-16, and ACTS (red lines) in the southernmost Ryukyu subduction zone. A vertical exaggeration of 2:1 is applied for 3-D visualization. Slab buckling (red surfaces) below the Hoping basement rise is seen in the western portion of the 3-D interfaces.

surfaces shown in Fig. 13). Along the profile of EW9509-1, the slab kink and an abrupt down-dip increase of the subduction angle are clearly seen. In order to tie together the crustal interfaces at the intersections of EW9509-1, EW9509-14 and EW9509-16, a wedge-shaped arc basement and a depression of the subducted slab are constructed although their constraints along EW9509-14 (a distance of 60-95 km in Fig. 8b) and EW9509-16 (a distance of 75-100 km in Fig. 9b) are limited. On the other hand, along profiles EW9509-14 and EW9509-16, warping of the arc basement and buckling of the subducted slab (the red surfaces in Fig. 13) in the western portion of the model are readily identified. Furthermore, the top and the bottom of the subducted slab along EW9509-16 are generally deeper than those along EW9509-14 and the difference of their slab depth is found to increase westward. These evidences again imply northward subduction and compression increasing westward at the termination point of the oblique subduction off NE Taiwan.

High seismicity below the forearc basins

The focal mechanisms of strong earthquakes are applied to compare the OBS velocity models and to study the seismicity in the forearc region since they have been used to efficiently delineate the crustal interfaces (Kao & Chen 1991; Kao *et al.* 1998). Several catalogues of the focal mechanisms, Harvard CMT, F-net in Japan and the Broadband Array in Taiwan for Seismology-BATS, have been updated, can be readily accessed and cover the Taiwan area. Among them, the epicenters of F-net and BATS are similar, while BATS provides the most complete coverage of events in the southernmost Ryukyu since 1996. Thus, we select the focal mechanisms given by Kao *et al.* (1998) and BATS for earthquakes having moment magnitudes greater than 5.5 in the southernmost Ryukyu. The earthquake mechanisms are then projected onto the OBS velocity models along profiles EW9509-1, EW9509-14 and EW9509-16 to compare with the structural interfaces.

Concerning the subduction boundary, the velocity contour of 6.75 km s^{-1} and the subduction angle of about 25 degrees in the OBS profile of EW9509-1 (Fig. 7b) are consistent with hypocentre locations and focal mechanisms indicating a shallow north dipping thrust plane. The subduction boundary at depths of 15–30 km could be the thrusting plane or the southern boundary of the earthquake mechanisms below the forearc basins. Similarly, an intracrustal interface, with a velocity contour of 6.75 km s^{-1} and southward dipping of about 35 degrees below the arc slope, is seen as the northern boundary of the thrust faulting. A southward dipping antithetic thrust may also exist below the arc slope although the focal planes of the fault-plane solutions are steeper than the intracrustal interface (Fig. 7b). According to the focal mechanisms along the Ryukyu arc from Japan to Taiwan, an antithetic thrust with an average dip of 15 degrees at depths of 15–25 km was also identified in the basement of the overriding plate (Kao & Chen 1991). They explained that the antithetic thrust in the arc basement is analogous to the antithetic thrusts of exhumed fold-and-thrust belts and modern accretionary wedges, with development in the hanging wall and at shallow depths. Therefore, the majority of the thrust faulting in the focal mechanisms below the forearc basins results not only from the PSP subduction underneae Ryukyu arc, but also from the backstop of the Ryukyu arc basement as demonstrated by the presence of an antithetic fault below the arc slope in the OBS velocity model along the profile of EW9509-1.

Earthquake swarms are found below the Nanao basin and beneath the Hoping basement rise (the inset of Fig. 1), but east of the Nanao basement rise is aseismic. Most earthquakes below the Nanao basin attribute to the thrust faulting along the plate interface and the antithetic fault in the basement of the overriding plate, while those beneath the Hoping basement rise may result from slab buckling (Figs 8b and 9b). We infer that, due to the oblique subduction and collision, the subducted slab near its northwestern edge buckles due to arc-parallel compression within the slab (Kao & Chen 1991), collision of the Luzon arc with the Ryukyu arc (Wang & Chiang 1998) or volcanism in the westernmost PSP. Fractures and dehydration observed from the anomalously high Poisson's ratio below the Nanao basin (Wang & Pan 2001) and the significant distortion of the plate interface toward its westernmost boundary (Kao *et al.* 1998) also support the presence of oblique thrust faulting and the slab buckling in the forearc region.

Previous earthquakes with moment magnitudes greater than 6.7 in the southernmost Ryukyu forearc region, labelled with their moment magnitudes in the inset of Figs 1, 8(b) and 9(b), occurred on 1966 March 12 ($M_w = 7.79$), 1967 October 25 ($M_w = 6.87$), 2001 December 18 ($M_w = 6.74$), and 2002 March 31 ($M_w = 6.84$). These strong earthquakes at the forearc are not associated with thrust faulting but reveal the strike-slip component of the faulting or arc-parallel compression due to oblique subduction. In particular, the earthquake on 2002 March 31 located below the Hoping basin, the most recent one and the closest one to Taiwan, hit the Taipei basin (having an epicentral distance of about 100 km) with a peak ground acceleration of more than 1 m s^{-2}. Arc-parallel buckling of the subducted slab below the Hoping basement rise proposed in this study may have resulted in this strong earthquake. Therefore, the velocity-interface models and the focal mechanisms in the southernmost Ryukyu suggest that strike-slip faulting due to slab buckling or arc-parallel compression has induced earthquakes stronger than those generated by thrust faulting along the subduction interface and the antithetic fault.

CONCLUSIONS

Layer-stripping Monte Carlo inversion of the crustal structure from three OBS/MCS profiles in the southernmost Ryukyu has been presented. The velocity uncertainty of the model is generally less than 0.25 km s^{-1} except below the Nanao basin, where it reaches 0.45 km s^{-1}. The uncertainty of the model interface is generally less than 0.5 km except at the Moho below the western portion of the Nanao basin.

Structural interfaces constructed from the OBS velocity models and the density models in the southernmost Ryukyu subduction zone show a wedge-shaped arc basement beneath the Yaeyama accretionary prism, an antithetic fault below the arc slope, and northward thickening of the arc basement beneath the southern portion of the Hoping basin. These features are mainly attributable to the northward subduction of the PSP, as also demonstrated by the prominent thrust faulting near the plate interface. On the other hand, due to the westward component of the oblique subduction and the on-going collision at the northwestern edge of the PSP, the arc-parallel buckling of the subducted slab, the warping of the arc basement and the formation of the Hoping basement rise between the Hoping and Nanao basins are imaged. Furthermore, based on the gravity modelling, the relatively low density of the buckling slab at the north is found about 100 kg m^{-3} greater than that at the south, which may also imply the stronger buckling of the slab at the front of the northward subduction of the PSP. The slab buckling and the warping of the arc basement have generated swarms of earthquakes with strike-slip faulting beneath the Hoping basement rise. A recent earthquake

with a moment magnitude of 6.84 was induced by the slab buckling and strongly affected cities within an epicentral distance of 100 km.

ACKNOWLEDGMENTS

REFERENCES

Christeson, G.L., McIntosh, K.D., Shipley, T.H., Flueh, E.R. & Goedde, H., 1999. Structure of the Costa Rica convergent margin, offshore Nicoya Peninsula, *J. geophys. Res.,* **104,** 25 443–25 468.

Font, Y., Liu, C.S., Schnurle, P. & Lallemand, S., 2001. Constraints on backstop geometry of the southwest Ryukyu subduction based on reflection seismic data, *Tectonophysics, 333,* 135–158.

Hagen, R.A., Duennebier, F.K. & Hsu, V., 1988. A seismic refraction study of the crustal structure in the active seismic zone east of Taiwan, *J. geophys. Res.,* **93,** 4785–4796.

Hyndman, R.D., Yamano, M. & Oleskevich, D.A., 1997. The seismogenic zone of subduction thrust faults, *The Island Arc,* **6,** 244–260.

Iwasaki, T. *et al.*, 1990. Crustal and upper mantle structure in the Ryukyu Island Arc deduced from deep seismic sounding, *Geophys. J. Int.,* **102,** 631–651.

Jarrard, R.D., 1986. Relations among subduction parameters, *Rev. Geophys.,* **24,** 217–284.

Kao, H. & Chen, W.P., 1991. Earthquakes along the Ryukyu-Kyushu Arc: strain segmentation, lateral compression, and the thermomechanical state of the plate interface, *J. geophys. Res.,* **96,** 21 443–21 485.

Kao, H., Shen, S.S.J. & Ma, K.F., 1998. Transition from oblique subduction to collision: Earthquakes in the southernmost Ryukyu arc-Taiwan region, *J. geophys. Res.,* **103,** 7211–7229.

Kodaira, S., Iwasaki, T., Urabe, T., Kanazawa, T., Egloff, F., Makris, J. & Shimamura, H., 1996. Crustal structure across the middle Ryukyu trench obtained from ocean bottom seismographic data, *Tectonophysics,* **263,** 39–60.

Kodaira, S., Takahashi, N., Park, J.O., Mochizuki, K., Shinohara, M. & Kimura, S., 2000. Western Nankai Trough seismogenic zone: Results from a wide-angle ocean bottom seismic survey, *J. geophys. Res.,* **105,** 5887–5905.

Lallemand, S., Liu, C.S., Dominguez, S., Schnürle, P., Malavieille, J., and the ACT Scientific Crew, 1999. Trench-parallel stretching and folding of forearc basins and lateral migration of the accretionary wedge in the southern Ryukyus: A case of strain partition caused by oblique convergence, *Tectonics,* **18,** 231–247.

Leitner, B., Trehu, A.M. & Godfrey, N.J., 1998. Crustal structure of the northwestern Vizcaino block and Gorda Escarpment, offshore northern California, and implications for postsubduction deformation of a paleoaccretionary margin, *J. geophys. Res.,* **103,** 23 795–23 812.

Lin, S.F., 2000. Sedimentary and crustal P-wave velocity structures in the southern Ryukyu forearc subduction zone, *M.S. Thesis* (in Chinese), Institute of Applied Geophysics, National Taiwan Ocean University, Taiwan, R.O.C.

Lin, C.H., Yeh, Y.H., Yen, H.Y., Chen, K.C., Roecker, S.W. & Chiu, J.M., 1998. Three-dimensional elastic wave velocity structure of the Hualien region of Taiwan: Evidence of active crustal exhumation, *Tectonics,* **17,** 89–103.

Liu, C.S., Schnürle, P., Lallemand, S.E. & Reed, D.L., 1997. TAICRUST and deep seismic imaging of western end of Ryukyu arc-trench system, in *Deep Sea Research in Subduction Zones, Spreading Centers and Backarc Basin, JAMSTEC J. Deep Sea Res.,* pp. 39–45, ed. Fujioka, K., JAMSTEC, Japan.

Liu, C.S., Liu, S.Y., Lallemand, S.E., Lundberg, N. & Reed, D.L., 1998. Digital elevation model offshore Taiwan and its tectonic implications, *Terr. Atmo. Ocea.,* **9,** 705–738.

McIntosh, K.D. & Nakamura, Y., 1998. Crustal structure beneath the Nanaoo forearc basin from TAICRUST MCS/OBS Line 14, *Terr. Atmo. Ocea.,* **9,** 345–362.

Park, J.O., Tokuyama, H., Shinohara, M., Suyehiro, K. & Taira, A., 1998. Seismic record of tectonic evolution and backarc rifting in the southern Ryukyu island arc system, *Tectonophysics,* **294,** 21–42.

Polet, J. & Kanamori, H., 2000. Shallow subduction zone earthquakes and their tsunamigenic potential, *Geophys. J. Int.,* **142,** 684–702.

Schnürle, P., Liu, C.S., Lallemand, S.E. & Reed, D.L., 1998. Structural insight into the south Ryukyu margin: Effects of the subducting Gagua Ridge, *Tectonophysics,* **288,** 237–250.

Spada, G., 2001. Mantle viscosity from Monte Carlo inversion of very long baseline interferometry data, *J. geophys. Res.,* **106,** 16 375–16 385.

Tsuru, T., Park, J.O., Takahashi, N., Kodaira, S., Kido, Y., Kaneda, Y. & Kono, Y., 2000. Tectonic features of the Japan Trench convergent margin off Sanriku, northeastern Japan, revealed by multichannel seismic reflection data, *J. geophys. Res.,* **105,** 16 403–16 413.

Wang, T.K. & Chiang, C.H., 1998. Imaging of arc-arc collision in the Ryukyu forearc region offshore Hualien from TAICRUST OBS Line 16, *Terr. Atmo. Ocea.,* **9,** 329–344.

Wang, T.K. & Pan, C.H., 2001. Crustal Poisson's ratio off eastern Taiwan from OBS data modelling, *Terr. Atmo. Ocea.,* **12,** 249–268.

Wang, T.K., McIntoish, K., Nakamura, Y., Liu, C.S. & Chen, H.W., 2001. Velocity-interface structure of the southwestern Ryukyu subduction zone from EW9509-1 OBS/MCS data, *Mar. Geophys. Res.,* **22,** 265–287.

Webring, M., 1985. SAKI: A fortran program for generalized linear inversion of gravity and magnetic profiles, *US Geology Survey,* 85–122, p. 29.

Wessel, P. & Smith, W.H.F., 1995. New version of the generic mapping tools (GMT) version 3.0 released, *EOS, Trans. Am. geophys. Un.,* **76,** 329.

Zaidi, H., 1999. Relevance of accurate Monte Carlo modelling in nuclear medical imaging, *Medical Physics,* **26,** 574–608.

Zelt, C.A. & Smith, R.B., 1992. Seismic traveltime inversion for 2-D crustal velocity structure, *Geophys. J. Int.,* **108,** 16–34.